Chemical Science

ROYAL SOCIETY OF CHEMISTRY

EDGE ARTICLE

View Article Online
View Journal | View Issue

Cite this: *Chem. Sci.*, 2023, **14**, 13067

All publication charges for this article have been paid for by the Royal Society of Chemistry

Surface modification of garnet fillers with a polymeric sacrificial agent enables compatible interfaces of composite solid-state electrolytes†

Bin Luo,[a] Jintian Wu,[ac] Ming Zhang,[a] Zhihao Zhang,[a] Xingwei Zhang,[a] Zixuan Fang, *[a] Ziqiang Xu*[ab] and Mengqiang Wu *[ab]

The poly (vinylidene fluoride) (PVDF)-based composite solid-state electrolyte (CSE) has garnered attention due to its excellent comprehensive performance. However, challenges persist in the structural design and preparation process of the ceramic-filled CSE, as the PVDF-based matrix is susceptible to alkaline conditions and dehydrofluorination, leading to its incompatibility with ceramic fillers and hindering the preparation of solid-state electrolytes. In this study, the mechanism of dehydrofluorination failure of a PVDF-based polymer in the presence of Li_2CO_3 on the surface of $Li_{6.4}La_3Zr_{1.4}Ta_{0.6}O_{12}$ (LLZTO) is analyzed, and an effective strategy is proposed to inhibit the dehydrofluorination failure on the basis of density functional theory (DFT). We introduce a molecule with a small LUMO–HOMO gap as a sacrificial agent, which is able to remove the Li_2CO_3 impurities. Therefore, the approach of polyacrylic acid (PAA) as a sacrificial agent reduces the degree of dehydrofluorination in the PVDF-based polymer and ensures slurry fluidity, promoting the homogeneous distribution of ceramic fillers in the electrolyte membrane and enhancing compatibility with the polymer. Consequently, the prepared electrolyte membranes exhibit good electrochemical and mechanical properties. The assembled Li-symmetric cell can cycle at 0.1 mA cm^{-2} for 3500 h. The $LiFePO_4$||Li cell maintains 91.45% of its initial capacity after 650 cycles at 1C, and the $LiCoO_2$||Li cell maintains 84.9% of its initial capacity after 160 cycles, demonstrating promising high-voltage performance. This facile modification strategy can effectively improve compatibility issues between the polymer and fillers, which paves the way for the mass production of solid-state electrolytes.

Received 6th September 2023
Accepted 26th October 2023

DOI: 10.1039/d3sc04710e

rsc.li/chemical-science

1 Introduction

With the new technological revolution, electric vehicles, electronic equipment and multi-modal energy storage have become indispensable in modern society. Therefore, people have put forward higher safety and energy density requirements for energy storage devices. Because of the excellent theoretical specific capacity, the lithium metal anode is under consideration for the next generation of lithium batteries.[1,2] In order to develop a suitable electrolyte, researchers have turned their attention to solid-state electrolytes (SSEs) as an alternative to organic liquid electrolytes to make solid-state lithium metal batteries, thereby significantly enhancing battery safety and energy density.[3]

The SSEs are categorized into solid-state polymeric electrolytes (SPEs), inorganic solid-state electrolytes (ISEs) and composite solid-state electrolytes (CSEs), based on the components.[4] CSEs are highly regarded for their combination of the excellent ionic conductivity and mechanical strength of ISEs, along with the low interfacial impedance of SPEs. The CSEs mainly consist of an inorganic filler, polymer matrix and lithium salt. Common polymer matrices include PEO, PVDF, PAN and PPC.[5] Among them, PVDF has been widely studied because of its good comprehensive performance, especially for its high dielectric constant (ε_r).[6,7] As for the inorganic fillers, they can be divided into inert fillers (*e.g.* SiO_2, Al_2O_3, TiO_2, ZrO_2, *etc.*) and active fillers (*e.g.* $Li_{6.4}La_3Zr_{1.4}Ta_{0.6}O_{12}$ (LLZTO), $Li_{1.5}Al_{0.5}Ti_{1.5}(PO_4)_3$, $Li_7Ge_2P_5S_{10}$, Li_3PS_4, *etc.*) according to their ability to conduct ions. Among them, garnet-type solid electrolyte LLTZO has excellent conductivity performance, high chemical stability and a good shear modulus.[8]

However, LLZTO is prone to reacting with water and CO_2 in an air atmosphere to form an alkaline layer of Li_2CO_3 on its surface, which leads to its lithiophobicity and a decrease in

[a]School of Materials and Energy, University of Electronic Science and Technology of China, Chengdu 611731, Sichuan, China. E-mail: zixuanfang@uestc.edu.cn; nanterxu@uestc.edu.cn; mwu@uestc.edu.cn

[b]Yangtze Delta Region Institute (HuZhou), University of Electronic Science and Technology of China, Huzhou 313001, Zhejiang, China

[c]School of Chemical Engineering, Sichuan University of Science & Engineering, Zigong 643000, China

† Electronic supplementary information (ESI) available. See DOI: https://doi.org/10.1039/d3sc04710e

conductivity.[9,10] Moreover, an alkaline environment resulting from the Li_2CO_3 layer on the LLZTO surface will cause dehydrofluorination of PVDF, which can be understood by using the following equation,[11]

$$2(CH_2–CF_2)_n + Li_2CO_3 \rightarrow 2(CH{=}CF)_n + 2LiF + H_2O + CO_2 \quad (1)$$

The generated C=C unsaturated bonds may cross-link and reduce the fluidity of the slurry or even gelate, resulting in the components not being homogeneously mixed,[12] which blocks the migration of Li^+, weakening the ionic transport and mechanical properties of CSE.[13,14] In addition, the formation of C=C bonds reduces the flexibility of the molecular chains, which increases the interfacial resistance of PVDF and the fillers.[14,15] Moreover, Yi *et al.* found that the defluorination of a PVDF-based polymer impairs the compatibility of the electrolyte membrane with electrodes,[15] and gelation is an obstacle to mass production in slurries with PVDF-based polymers.[5,15,16] Various strategies such as rapid acid treatment,[17] using high-temperature decomposition[18] and high-speed mechanical polishing[19] have been proposed to solve these problems. More recently, Lee *et al.* employed dry etching to treat the surface of LLZO to remove Li_2CO_3.[20] This treatment promoted the formation of fast Li^+ conductive pathways along the LLZO fillers. The composite electrolyte membrane prepared with a PVDF matrix has good ionic conductivity and electrochemical properties. However, dry etching may lead to a potential risk of partial transition of cubic LLZO into the tetragonal phase. In addition, these methods are too complex and expensive. Therefore, it is critical to develop a facile design strategy to enhance compatibility among components based on CSEs.

In this work, we introduce polyacrylic acid (PAA) with a smaller LUMO–HOMO gap than poly (vinylidene fluoride-*co*-chlorotrifluoroethylene) (P(VDF-CTFE)) as a sacrificial agent to modify the surface of LLZTO by DFT analysis. The CSEs with ceramic fillers and P(VDF-CTFE) are prepared by the solution casting method. According to the DFT, the oxygen atom in the carboxyl group of PAA is the main electrophilic site, leading to the reaction of PAA with Li_2CO_3 on the surface of LLZTO. The degree of dehydrofluorination of P(VDF-CTFE) is reduced owing to the removal of alkaline substances, thus avoiding a decrease in the fluidity of the slurry that would prevent the coating of the membrane. The modifications improve the compatibility between the ceramic and matrix and ensure the homogeneous distribution of the filler, facilitating fast and uniform Li^+ transport. Therefore, the prepared P(VDF-CTFE)@LLZTO-PAA CSE exhibits an excellent ionic conductivity of 4.53×10^{-4} S cm^{-1}, a Li^+ transfer number of 0.336 and an enlarged electrochemical window of 4.5 V (*vs.* Li^+/Li). The as-assembled Li‖P(VDF-CTFE)@LLZTO-PAA CSE‖$LiFePO_4$ can stably cycle 650 times at 1C with an initial specific discharge capacity of 143.8 mA h g^{-1}, and has a capacity retention of 91.45%. This study presents a facile and effective approach for modifying alkaline ceramic fillers to be compatible with polymeric matrices and the large-scale preparation of composite solid-state electrolytes, which have excellent potential for mass production in the industry.

2 Results and discussion

2.1. Modification process of the ceramic filler surface

To study the mechanism of LLZTO modification by using a PAA sacrificial agent, Fig. 1(a) shows the schematic synthesis process of LLZTO-PAA filler particles. As shown in Fig. 1(a), PAA is introduced onto the surface of LLZTO. To further understand the reactions during the modification process, the LLZTO particles, PAA powder and LLZTO-PAA particles are characterized by using FTIR (Fig. 1(b)). The characteristic peak at 864 cm^{-1} corresponding to CO_3^{2-} appears in the FTIR spectrum of LLZTO,[17,21] which is attributable to the reaction among water, CO_2 and the Li^+ of LLZTO.[9,10] Hence, it is inevitable to observe Li_2CO_3 on the surface of LLZTO. As for the PAA powder, the peaks at 2961 and 1172 cm^{-1} are attributed to the asymmetric stretching vibration mode of –CH_2 and the stretching vibration of C–O, respectively; the absorption peak at 1716 cm^{-1} is related to the stretching vibration mode of C=O in the –COOH group.[22] When LLZTO is modified by PAA, the peak at 864 cm^{-1} disappears, and the intensity of the peak at 1716 cm^{-1} decreases. Meanwhile, two new peaks appear at 1567 and 1416 cm^{-1}, attributed to the symmetric and asymmetric stretching vibrational modes in –COO^-, respectively.[23,24] The peak located at 2942 cm^{-1} is related to the characteristic peak of the –CH_2 group of PAA.

It is generally considered that the vibration modes of the organic functional group are very sensitive to the Raman spectra, and Fig. 1(c) displays the characterization results for LLZTO, PAA and LLZTO-PAA. As depicted in Fig. 1(c), similar phenomena are observed in the Raman spectra. First, the peak belonging to the carboxyl group at 1670 cm^{-1} can be found in the spectrum of PAA, and the characteristic peaks corresponding to the vibration mode of –CH_2 and the stretching mode of –CH_2 or –CH can be found at 1100 and 2936 cm^{-1}, respectively.[22,25] As for the spectrum of LLZTO, the peaks at 294, 370, 684 and 771 cm^{-1} are attributed to the garnet phase, which can also be found in the spectrum of LLZTO-PAA, indicating that the modulation of the PAA sacrificial agent does not change the cubic structure of the ceramics.[17] In particular, the peak at 1086 cm^{-1} associated with carbonate vibration which further demonstrates the presence of Li_2CO_3. In contrast, after PAA modification, the vibrational peak of Li_2CO_3 disappears from the LLZTO-PAA spectra, indicating that the alkaline contaminated layer is removed from the surface of LLZTO. The peak at 1670 cm^{-1} associated with the carboxyl group disappears, but a new peak corresponding to the symmetric vibration of –COO^- appears at 1423 cm^{-1} and a peak belonging to –CH_2 or –CH is present at 2926 cm^{-1}.[26] Both FTIR and Raman spectra indicate that the surface treatment of LLZTO can effectively remove Li_2CO_3 content. Specifically, the carbonate group on the surface of LLZTO will react with the carboxyl group of PAA, which is represented by the following equation,

$$CO_3^{2-} + 2 - COOH \rightarrow 2COO^- + H_2O + CO_2 \quad (2)$$

The strategy of surficial modification by a sacrificial agent is effective to remove the alkaline and low-conducting Li_2CO_3

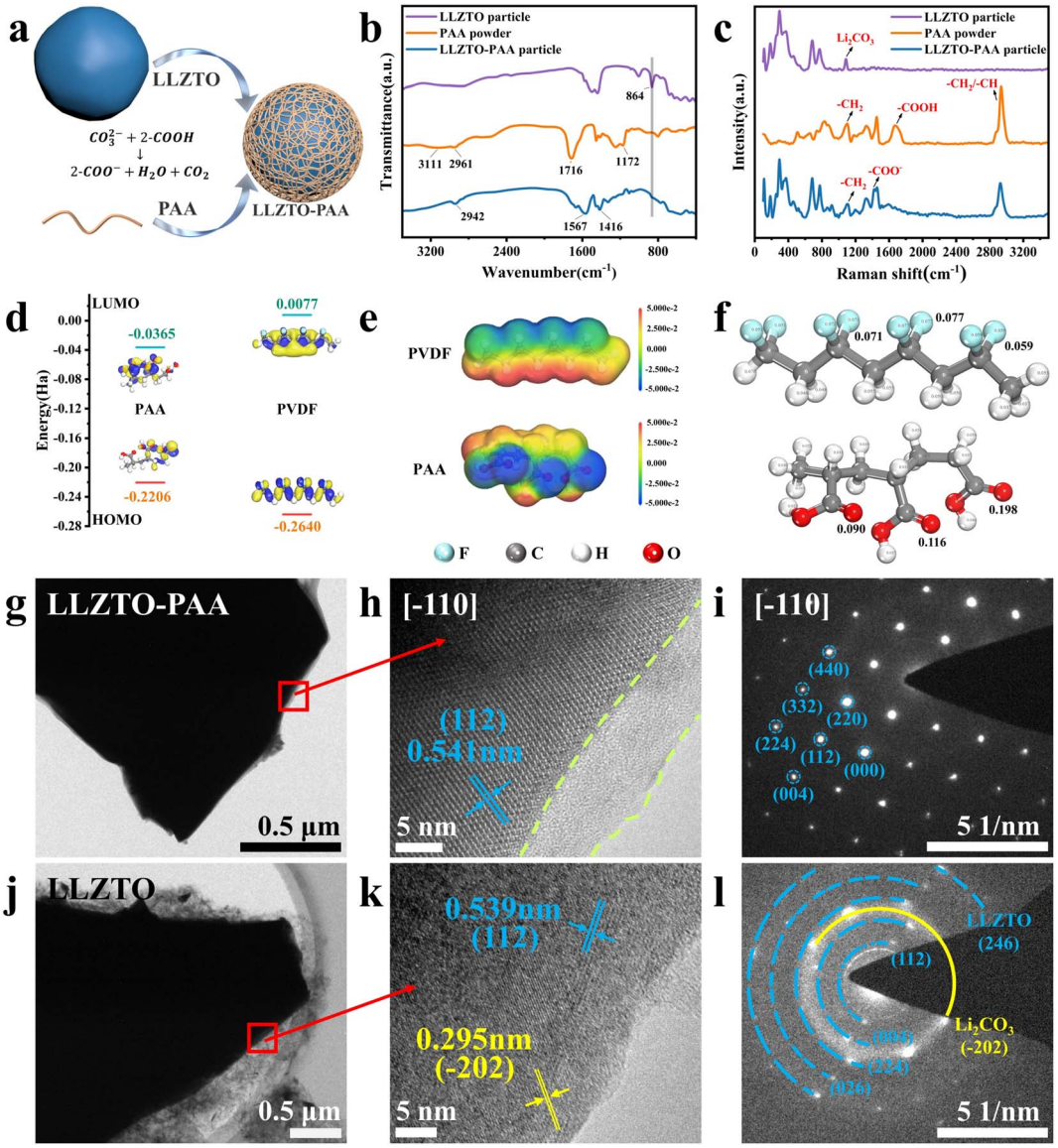

Fig. 1 (a) Schematic of the synthesis of the LLZTO-PAA filler. (b) FTIR spectra and (c) Raman spectra of the LLZTO particle, PAA powder and LLZTO-PAA filler particle. (d) LUMO and HOMO calculations for the PVDF fragment and PAA, where PVDF is the selected fragment from P(VDF-CTFE) that participates in the reaction. (e) The visualization images of electrostatic potential and (f) the electrophilic Fukui functions of the PVDF fragment and PAA. TEM images of (g) LLZTO-PAA and (j) LLZTO. HR-TEM images of (h) LLZTO-PAA and (k) LLZTO. SAED patterns of (i) LLZTO-PAA and (l) LLZTO. The [−110] in (h) and (i) is the zone axis.

from the ceramic surface, which is beneficial to ensure the ionic conductivity of LLZTO. The results of exploring suitable pH values by using different weight ratios of LLZTO/PAA are shown in Fig. S1.† The initial solution of LLZTO has a pH of 10.10, which gradually decreases with the addition of PAA. When the weight ratio is 3 : 1, the pH of the mixture decreases to 7.28, and PAA essentially neutralizes the alkalinity of LLZTO.

In order to further investigate the rationality of PAA as a sacrificial agent, the properties of PVDF fragments and PAA are studied, and the energy values of the LUMO and HOMO of the PVDF fragment and PAA are calculated by using DFT, respectively (Fig. 1(d)). PAA exhibits a smaller LUMO–HOMO gap of 0.1841 Ha than the PVDF fragment (0.2717 Ha), indicating that it is more susceptible to redox reactions and electron gain/loss. Meanwhile, combining the results of FTIR and Raman experiments, PAA is considered suitable to be used as a sacrificial agent to remove Li_2CO_3, and can inhibit the dehydrofluorination of the matrix. To further determine the electrophilic and nucleophilic sites, the electrostatic potentials (EPS) of the PVDF fragment and PAA are calculated and the distribution results of EPS on the molecular surfaces are visualized (Fig. 1(e)). It can be observed that the oxygen atoms in the carboxyl groups of PAA exhibit significantly negative electrostatic potential, primarily due to the strong contribution of its lone pair of electrons to the electrostatic potential. The calculated results of the electrophilic Fukui functions of the PVDF

fragment and PAA shown in Fig. 1(f) also indicate that the oxygen atom in the carboxyl group is the main electrophilic site. The results showed that the PAA sacrificial agent is more prone to excitation, and its carboxyl group can effectively react with Li_2CO_3 and reduce its initiated dehydrofluorination reactions, inhibiting the cross-linking of the matrix, which facilitates uniform dispersion of the components in the CSE membrane and enhances ionic conductivity and mechanical properties.

The microstructure of the LLZTO-PAA particles is analyzed by TEM. The LLZTO-PAA particle has a core–shell structure with a 10–20 nm polymer shell layer attached to the surface of the LLZTO ceramic core (Fig. S2†). As shown in Fig. 1(g and h), a dense amorphous shell layer can be clearly observed, which clings to the ceramic surface (as marked by the green dash lines). The lattice fringe with a spacing of 0.541 nm is measured and displayed in Fig. 1(h), which is well matched to the (112) lattice plane of LLZTO.[8,19] However, as for LLZTO without surficial treatment, the floccules are distributed on the surface of LLZTO particles (Fig. 1(j)), which may be correlated with the dislodged Li_2CO_3 during stirring. The lattice fringes are not uniformly arranged, and the lattice plane of (−202) with a lattice spacing of 0.295 nm belonging to Li_2CO_3 can be identified (Fig. 1(k)).[27] The selected-area electron diffraction (SAED) patterns are also different between LLZTO-PAA and LLZTO. The SAED pattern of LLZTO-PAA exhibits the diffraction spots of the (112), (220), (332), and (004) crystalline planes that are related to the cubic phase of LLZTO (Fig. 1(i)). In contrast, the SAED pattern of LLZTO exhibits a series of diffraction rings, and in particular the (−202) lattice plane attributed to Li_2CO_3 is again observed (Fig. 1(l)). To investigate the distribution of PAA on the LLZTO surface, EDS mapping of LLZTO-PAA particles is performed (Fig. S3†), where it is observed that PAA can coat LLZTO particles.

2.2. Morphology of SSE membranes and distribution of fillers

The prepared SSEs membranes are exhibited in Fig. 2(a–c), and the inset images of SSEs show that the membranes can be bent at large angles, which demonstrates their good flexibility. The P(VDF-CTFE) SPE membrane is translucent, but the color of the P(VDF-CTFE)@LLZTO CSE membrane turns brown with the addition of LLZTO, which is attributable to the fact that P(VDF-CTFE) undergoes the dehydrofluorination process. The fast dehydrofluorination process will reduce the fluidity of the solution of P(VDF-CTFE) with a LLZTO filler soon, and irreversibly transforms it into a gel state (Fig. S4†), making the coating process uncontrollable and leading to inhomogeneous dispersion of the fillers.[15,28] However, the color of the P(VDF-CTFE)@LLZTO-PAA CSE membrane is white and consistent with that of the LLZTO particles. This finding indicates that the alkalinity of LLZTO is suppressed (Fig. S1†). SEM images of the top view and cross section of the various electrolyte membranes are shown in Fig. 2(d–i). The appearance of small pores on the surface of the P(VDF-CTFE) SPE membrane may be attributable to the phase separation of the components as a result of solvent evaporation during the preparation of the membrane (Fig. S5†).[29] In contrast, an inhomogeneous and porous morphology of the internal CSE membrane with the direct addition of pure LLZTO ceramic particles is observed, which is attributable to the decrease in the fluidity of the slurry caused by the dehydrofluorination of P(VDF-CTFE). A homogeneous and dense morphology of LLZTO interconnected with the polymer matrix is observed on the surface of the P(VDF-CTFE)@LLZTO-PAA CSE membrane. This finding indicates that the morphology of membranes with PAA-modified ceramics is improved and becomes dense, facilitating the construction of a continuous Li^+ transport pathway based on the polymer matrix and increasing the ionic conductivity of CSE.[3,30]

To investigate the distribution of LLZTO in the SSE membrane, EDS mappings are performed on the cross section of the membrane, as shown in Fig. S6.† The distribution of the La element from LLZTO in the P(VDF-CTFE)@LLZTO-PAA CSE membrane is more uniform than that of the P(VDF-CTFE)@LLZTO CSE membrane, confirming the improvement of the distribution of ceramic fillers in the polymer matrix after PAA sacrificial agent modification. This result is probably related to the high compatibility of LLZTO-PAA with the polymer matrix and a lower degree of dehydrofluorination of P(VDF-CTFE), which allows for the homogeneous distribution of LLZTO in PVDF and facilitates the fluidity of the slurry to be maintained.

2.3. Interaction of components in SSE membranes

XRD curves of the prepared electrolyte membranes and fillers are shown in Fig. 3(a). First, the spectrum of the LLZTO particles is well matched to the standard card #45-0109, indicating that a pure cubic phase is observed, and PAA modification does not change the cubic phase of LLZTO.[5] The corresponding spectrum of P(VDF-CTFE) SPE exhibits two weak peaks at about 36.4° and 39.2°, as well as a broad characteristic peak at about 20.1° and a small peak at 22.1°, which are attributed to P(VDF-CTFE), which could verify the semi-crystalline phase of the polymer matrix.[31] With the addition of LLZTO-PAA, the diffraction peak positions of the P(VDF-CTFE) matrix and LLZTO in P(VDF-CTFE)@LLZTO-PAA CSE do not change. Moreover, in the spectra of the CSE, it is notable that the intensity of the diffraction peaks in the crystalline region of the P(VDF-CTFE) matrix decreases, and its peak located at 22.1° disappears, which may be attributable to the fillers disrupting the ordered arrangement of the polymer matrix.[31]

FTIR is used to explore the chemical structure and bonding transitions of the SSEs, as exhibited in Fig. 3(b). As for P(VDF-CTFE) SPE, peaks related to the vibration of the α-phase at 746 and 878 cm^{-1} are observed, and the peaks at 831, 1071, 1175, 1254 and 1379 cm^{-1} are correlated with the vibration of the β-phase.[32] Among them, the absorption peaks located at 1175 cm^{-1} originated from the $–CF_2$ vibration, which corresponds to 1166 cm^{-1} in the pure P(VDF-CTFE) membrane,[33,34] due to the interaction of the polymer with the lithium salt.[30] Meanwhile, the dissociation of LiFSI in P(VDF-CTFE) leads to new peaks at 1653 and 570 cm^{-1}. Meanwhile, the β-phase content is calculated from the absorption intensities located at 746 and 831 cm^{-1} by using the equation (ESI†), and the results

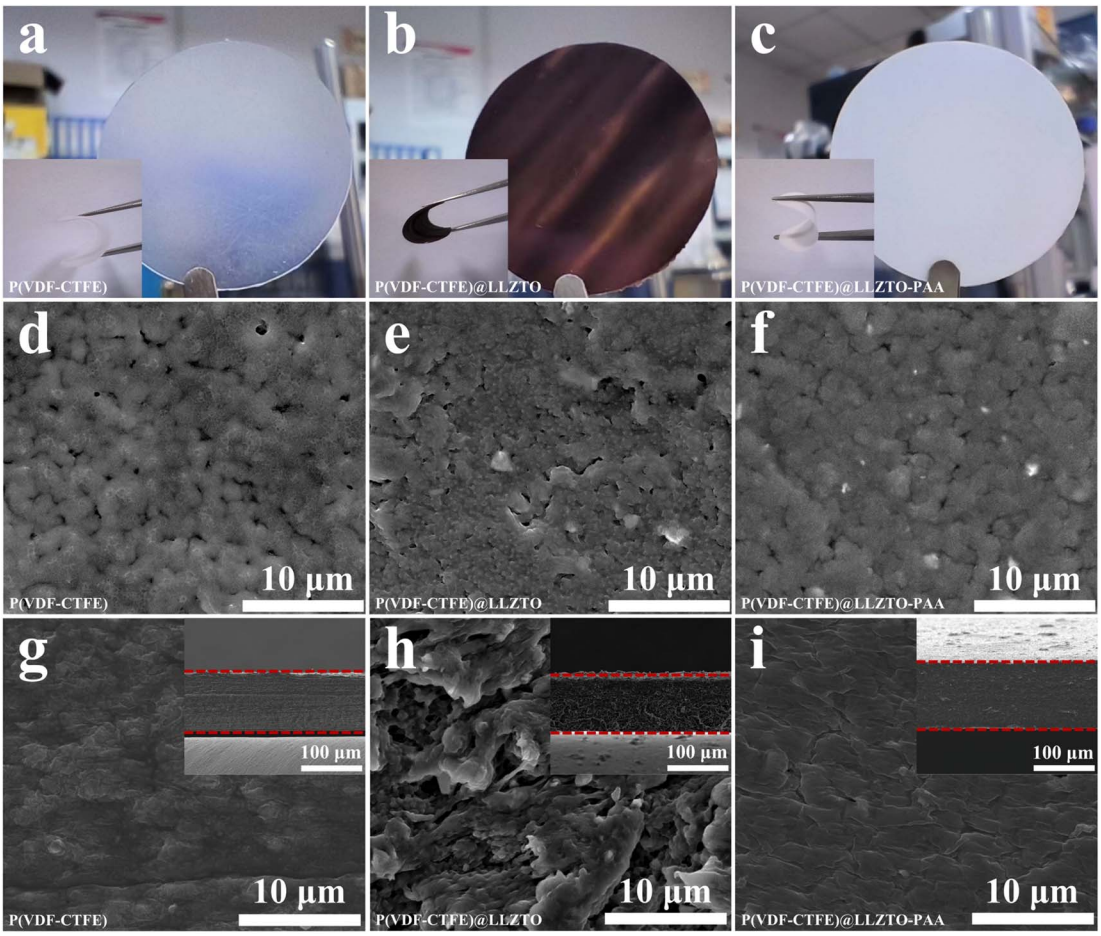

Fig. 2 P(VDF-CTFE) SPE: (a) optical image, (d) morphologies of the surface and (g) cross section; P(VDF-CTFE)@LLZTO CSE: (b) optical image, (e) morphologies of the surface and (h) cross section; P(VDF-CTFE)@LLZTO-PAA CSE: (c) optical image, (f) morphologies of the surface and (i) cross section. The insets of (a)–(c) show the bent SSE membranes. The insets of (g)–(i) show the entire cross section.

are shown in Table 1. When LLZTO-PAA is added, the β-phase content increases, which means the interaction between the fillers and P(VDF-CTFE).[32] Moreover, the β-phase has high polarity (ε_r = 10–13), which facilitates the dissociation of the lithium salt.[35] In addition, the Lewis acid–base interactions between the LLZTO fillers and the lithium salt also affect the dissociation of LiFSI.[36] The changes in the β-phase content are also observed in P(VDF-CTFE)@LLZTO CSE and P(VDF-CTFE)@PAA SPE. The increase of the β-phase in P(VDF-CTFE)@PAA SPE is probably caused by the effect of carboxylic acid groups in PAA on the solidification process of the polymer matrix. However, the β-phase content in P(VDF-CTFE)@LLZTO CSE does not change significantly compared to that of the P(VDF-CTFE) SPE, which is related to the reason that the fillers do not fully come into contact with the polymer due to its inhomogeneous distribution and agglomeration.

The DSC measurements are carried out to explore the melting temperature (T_m) and other thermodynamic parameters of the prepared SSE membranes. As shown in Fig. 3(c), the T_m is marked above the DSC curve of the corresponding SSE membranes. In comparison to the P(VDF-CTFE) SPE (161.70 °C), the T_m of the other three SSEs with additives decreases. P(VDF-CTFE)@LLZTO-PAA CSE has the lowest T_m (152.56 °C). According to equations (ESI†), the crystallinity (χ_c) of the corresponding SSE membranes is calculated (Table 1). The crystallinity of P(VDF-CTFE)@LLZTO CSE (21.30%) is higher than that of P(VDF-CTFE)@LLZTO-PAA CSE (14.94%). This finding is attributable to the non-uniform distribution of LLZTO fillers without surficial treatment in the polymer matrix, and its perturbing effect on the polymer chain segments is not significant.[30] The χ_c of P(VDF-CTFE)@LLZTO CSE is not much different from that of the SSE membrane without a filler (21.34%), which could not contribute significantly to the transport of Li^+. Furthermore, this finding suggests that the addition of LLZTO-PAA can effectively decrease the crystallinity of P(VDF-CTFE), which means an increase in the amorphous regions and enhanced chain segment movement within the matrix, leading to improvement of the transport of Li^+ and an increase in ionic conductivity.[21]

Raman spectroscopy is an effective technique for studying structures containing conjugate C=C double bonds, which are a sign of dehydrofluorination.[37] As shown in Fig. 3(d), there are two main changes in the spectra of P(VDF-CTFE)@LLZTO CSE without PAA modulation compared to those of P(VDF-CTFE)

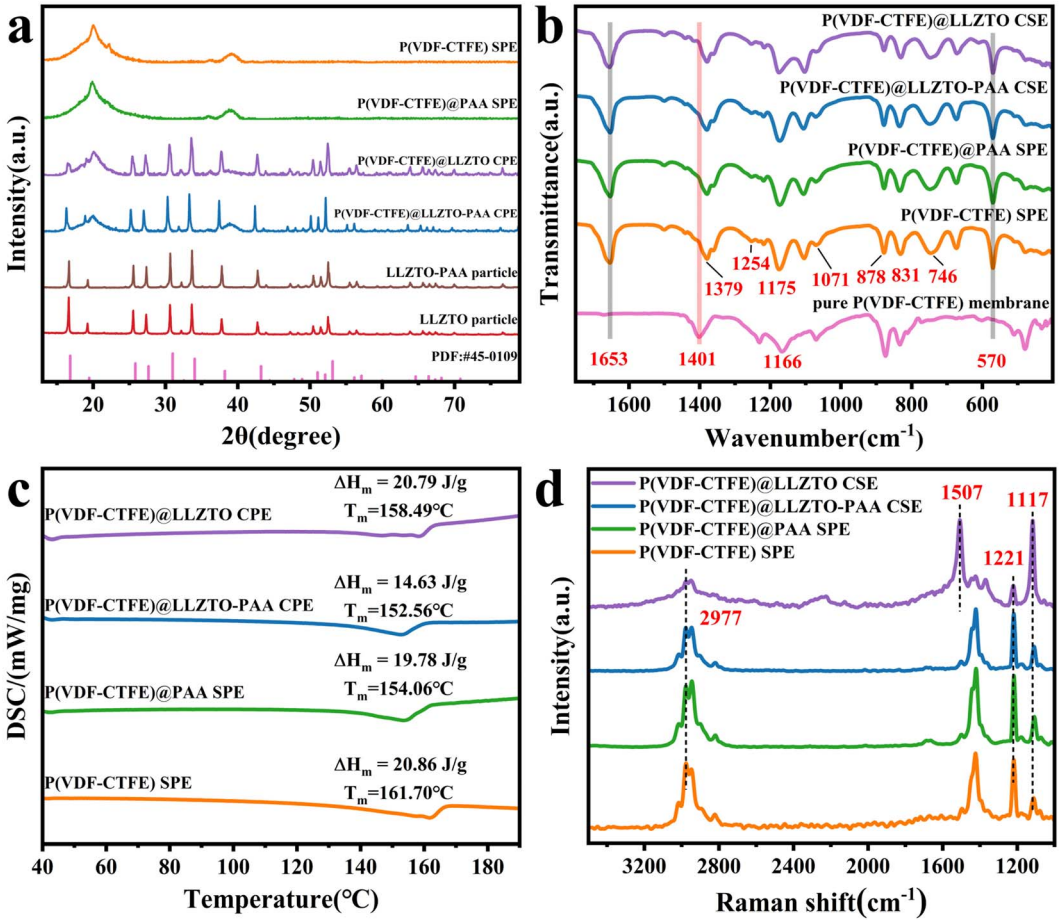

Fig. 3 (a) XRD curves of SSE membranes and ceramic fillers. (b) DSC heating curves, (c) FTIR spectra and (d) Raman spectra of SSE membranes.

Table 1 Thermal and crystalline properties of SSE membranes

SSE membrane	F (β) (%)	T_m (°C)	ΔH_m (J g^{-1})	χ_c (%)
P(VDF-CTFE)	45.37	161.70	20.86	21.34
P(VDF-CTFE)@LLZTO	44.93	158.49	20.79	21.30
P(VDF-CTFE)@PAA	46.38	154.06	19.78	20.22
P(VDF-CTFE)@LLZTO-PAA	47.17	152.56	14.63	14.94

SPE. The first change is the appearance of two new spectral bands at 1507 and 1117 cm^{-1}, which are signatures of the polyene C=C stretching vibrational mode. This phenomenon indicates that the polymer P(VDF-CTFE) has undergone a dehydrofluorination process to generate a conjugate C=C double bond structure under the influence of alkaline LLZTO.[38] In order to investigate the interaction between the PVDF fragment and Li_2CO_3, theoretical calculations are carried out for the system using DFT (Fig. S7†), and a strong interaction is observed between the PVDF fragment and Li_2CO_3 with an interaction energy of −1.24 eV. As displayed by the results in Fig. S7(b),† the length of the C–F bond (L_{C-F}) of the PVDF fragment after adsorption is elongated to about 1.53 Å from 1.36 Å, indicating the obvious trend of defluorination, which is consistent with the Raman test results. The second change is a substantial decrease in intensity located at 1432 and 2977 cm^{-1}, corresponding to the –CH tension vibrational and –CH_2 bending modes, respectively.[39] This finding indicates a decrease in –CH_2 groups in an alkaline environment. In contrast, the above two changes are not found in P(VDF-CTFE)@LLZTO-PAA CSE after the addition of a PAA sacrificial agent, and its Raman spectrum is almost identical to that of the P(VDF-CTFE) SPE and P(VDF-CTFE)@PAA SPE. This result indicates that surficial modification of LLZTO with PAA can inhibit the dehydrofluorination of the P(VDF-CTFE) matrix, which could improve the fabrication process of the electrolyte membrane.[11]

2.4. Performance of SSEs

Studies have shown that the concentration of ceramic fillers significantly affects the ionic conductivity (σ) of SSEs. At a given LLZTO/PAA ratio of 3 : 1.2, different concentrations of LLZTO-PAA fillers are added to P(VDF-CTFE). The ionic conductivity of P(VDF-CTFE)@LLZTO-PAA CSEs with varying ceramic contents is shown in Fig. S8.† In the CSEs, the weight ratios of the P(VDF-CTFE) matrix and LLZTO-PAA fillers are 10 : 1, 5 : 1, 10 : 3 and 5 : 2, and the corresponding room temperature σ is measured to be 4.53 × 10^{-4}, 1.21 × 10^{-4}, 9.25 × 10^{-5}, and 6.40 × 10^{-5} S cm^{-1}, respectively. Moreover, all of these CSEs have an electrochemical window of about 4.5 V, and exhibit good

electrochemical stability (Fig. S9†). However, when excess amounts of ceramic fillers are added, agglomeration of LLZTO will occur, and this will inevitably deteriorate the capability of ion transportation. Therefore, the optimal weight ratio of P(VDF-CTFE) to LLZTO is 10 : 1.

To study the ion transport in CSE membranes, the σ of the various membranes is shown in Fig. 4(a). The weight ratios of P(VDF-CTFE) to LLZTO and LiFSI are identified to be 10 : 1 and 3 : 2 (Fig. S10†), respectively. The σ of P(VDF-CTFE)@PAA SPE is 2.73×10^{-4} S cm^{-1}, slightly surpassing that of P(VDF-CTFE) SPE (2.53×10^{-4} S cm^{-1}), owing to the reduced crystallinity of the polymer matrix and the contribution of the carboxyl group to Li^+ transport.[39] Moreover, the σ of P(VDF-CTFE)@LLZTO-PAA CSE (4.53×10^{-4} S cm^{-1}) is significantly higher compared to that of P(VDF-CTFE)@LLZTO CSE (1.93×10^{-4} S cm^{-1}). This difference can be attributed to the uniform distribution of LLZTO-PAA, leading to a decrease in the crystallinity of P(VDF-CTFE) and the formation of a fast Li^+ transport pathway dominated by the polymer matrix.[40,41] Based on the above analysis and characterization results, the increase in conductivity of P(VDF-CTFE)@LLZTO CSE is mainly related to the following factors: (1) the dense structure of the membrane and the homogeneous distribution of the fillers facilitate the continuous transport of Li^+; (2) the addition of LLZTO-PAA effectively reduces the crystallinity of P(VDF-CTFE), which promotes the migration of Li^+.[40] In addition, Fig. 4(b) shows the Arrhenius curves for different electrolyte membranes, where the σ of all the SSE membranes increases with increasing temperature due to the increased ability of the chain segments of the polymer matrix to move. It is observed that P(VDF-CTFE)@LLZTO-PAA CSE exhibits a minimum E_a of 0.206 eV, indicating that the Li^+ can migrate through it with a lower migration barrier. In contrast, the E_a of P(VDF-CTFE)@LLZTO CSE is 0.256 eV, which may be related to the agglomeration and inhomogeneous distribution of the ceramic fillers in the CSE.[42]

The electrochemical window is a crucial parameter for assessing the electrochemical stability of an electrolyte. Fig. 4(c) shows the results of linear scanning voltammetry (LSV) measurements on electrolyte membranes. P(VDF-CTFE)@LLZTO CSE has an electrochemical window of 4.3 V (*vs.* Li^+/Li). The electrochemical window for P(VDF-CTFE) SPE and P(VDF-CTFE)@PAA SPE is 4.1 V, which is less than that reported in other literature studies,[43] attributed to the effect of residual solvent (Fig. S11†).[44] Significantly, the P(VDF-CTFE)@LLZTO-PAA CSE exhibits a higher oxidation decomposition voltage of 4.5 V, which may be attributable to a more homogeneous distribution of ceramics and restrain activity of DMF.[33,40,45] The enhanced electrochemical stability enables the electrolyte to effectively match with a high-voltage cathode to provide high energy density.

Good mechanical properties are essential for the safe use of SSE-based lithium batteries in practice, and are related to the ability of the electrolyte membrane to inhibit lithium dendrites. The mechanical performances of SSE membranes are evaluated by using stress–strain curves (Fig. 4(d)). The tensile strength (TS) of P(VDF-CTFE) SPE is 2.79 MPa and the maximum strain is 27.24%. The TS of P(VDF-CTFE)@LLZTO CSE is only 0.554 MPa after adding pure LLZTO due to the agglomeration of ceramics and poor film formation. However, with the addition of LLZTO-PAA, P(VDF-CTFE)@LLZTO-PAA CSE possesses a TS of 5.22 MPa and a maximum strain of 79.93%. These improved mechanical properties are due to the adhesion between the P(VDF-CTFE) matrix and the ceramic filler. Thus, the addition of LLZTO-PAA endows the electrolyte membrane with better mechanical stability to support the safety of the battery.[33]

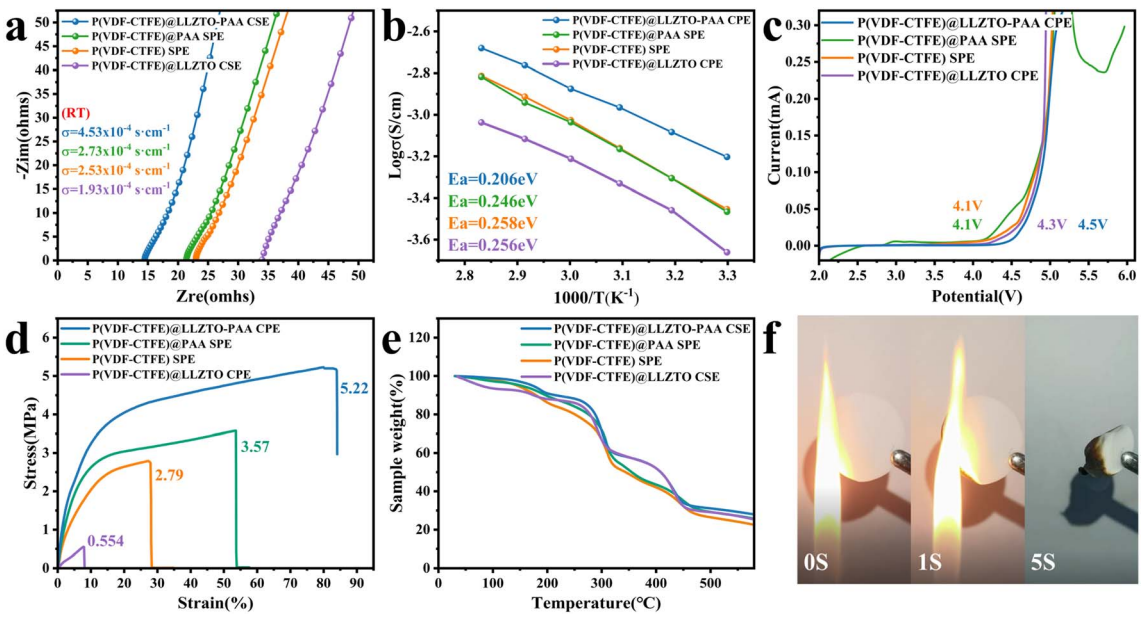

Fig. 4 (a) The EIS curves of SSE membranes. (b) Arrhenius plots of ionic conductivities of SSE membranes. (c) LSV curves, (d) stress–strain curves and (e) TGA curves of SSE membranes. (f) Flammability tests of P(VDF-CTFE)@LLZTO-PAA CSE.

Thermogravimetric analysis (TGA) conducted from 30 °C to 600 °C is performed to assess the thermal stability of the electrolyte membrane (Fig. 4(e)), which is also an essential factor regarding battery safety. The weight loss trend is consistent for all SSEs. The weight losses observed within the temperature ranges of 310 °C to 450 °C and 200 °C to 310 °C are caused by the decomposition of P(VDF-CTFE) and lithium salt, respectively.[46] Trace amounts of water retention contribute to weight loss before 55 °C. Moreover, the weight loss between 55 °C and 195 °C can be attributed to the residual solvent DMF.[6] Therefore, the amount of DMF can be roughly calculated to be approximately 12.3%, 9.2%, 8.9% and 8.3% in P(VDF-CTFE) SPE, P(VDF-CTFE)@LLZTO CSE, P(VDF-CTFE)@PAA SPE and P(VDF-CTFE)@LLZTO-PAA CSE, respectively. The flammability test is used to assess the safety of electrolyte films further. As depicted in Fig. 4(f), P(VDF-CTFE)@LLZTO-PAA CSE does not continue to burn after being heated by a heat source, which demonstrates its good thermal safety.

2.5. Performance and characterization of Li||SSEs||Li cells

The Li^+ transference number (t_{Li^+}) is an essential parameter for evaluating the Li^+ transport capacity of the electrolyte. Fig. 5(a) and S12† show the constant potential polarization process and the corresponding impedance spectrum of the lithium symmetric cell assembled from SSEs. The t_{Li^+} values for P(VDF-CTFE) SPE and P(VDF-CTFE)@PAA SPE are calculated to be 0.176, 0.172, respectively, according to the equation (ESI†). Moreover, the t_{Li^+} values for P(VDF-CTFE)@LLZTO CSE and P(VDF-CTFE)@LLZTO-PAA CSE are 0.167 and 0.336, respectively. The agglomerated ceramics could not form fast Li^+ channels, and their contact area with the anion is reduced, which results in a lower t_{Li^+}.[47] In contrast, as for the P(VDF-CTFE)@LLZTO-PAA CSE, the enhanced t_{Li^+} is attributed to the high ionic conductivity of LLZTO and its immobilization of the FSI^- anion.[48] A high t_{Li^+} facilitates the reduction of the concentration polarization during charging/discharging, and enables the diffusion and uniform precipitation of Li^+.

The Li||SSEs||Li symmetric cells are assembled and tested for constant current cycling to investigate the ability of SSEs to inhibit lithium dendrite growth. Fig. 5(b) shows the lithium plating and stripping behavior of the cells under the conditions of 25 °C and 0.1 mA cm^{-2}. The cycle life of the cells with P(VDF-CTFE) SPE and P(VDF-CTFE)@PAA SPE is 1600 h and 2050 h, respectively. It is reported that the Li polyacrylic acid (LiPAA) formed by the PAA^- anion and Li^+ could improve the electrolyte's ability to resist volume changes in the lithium anode.[31,49] The Li||P(VDF-CTFE)@LLZTO CSE||Li cell produces a huge polarization voltage after 850 h of cycling and the cell eventually fails in an open circuit mode. The failure here could be attributable to the lower t_{Li^+}, which causes anions to accumulate at the interface and form a space charge layer, resulting in a greater interfacial impedance.[50] Interestingly, the Li||P(VDF-CTFE)@LLZTO-PAA CSE||Li cell maintains a stable polarization voltage over a 3500 h cycle, indicating its enhanced stability towards lithium metal and effective inhibition of lithium dendrite growth. As depicted in Fig. 5(c), the critical current density of Li||P(VDF-CTFE)@LLZTO-PAA CSE||Li is 0.6 mA cm^{-2}, which exceeds that of Li||P(VDF-CTFE)@LLZTO CSE||Li (0.4 mA cm^{-2}). The microscopic morphology of the lithium metal surface after cycling Li||SSEs||Li for 200h is observed by using SEM (Fig. 5(d and e)). The lithium surface of Li||P(VDF-CTFE) SPE||Li exhibits roughness and non-uniformity, while Li||P(VDF-

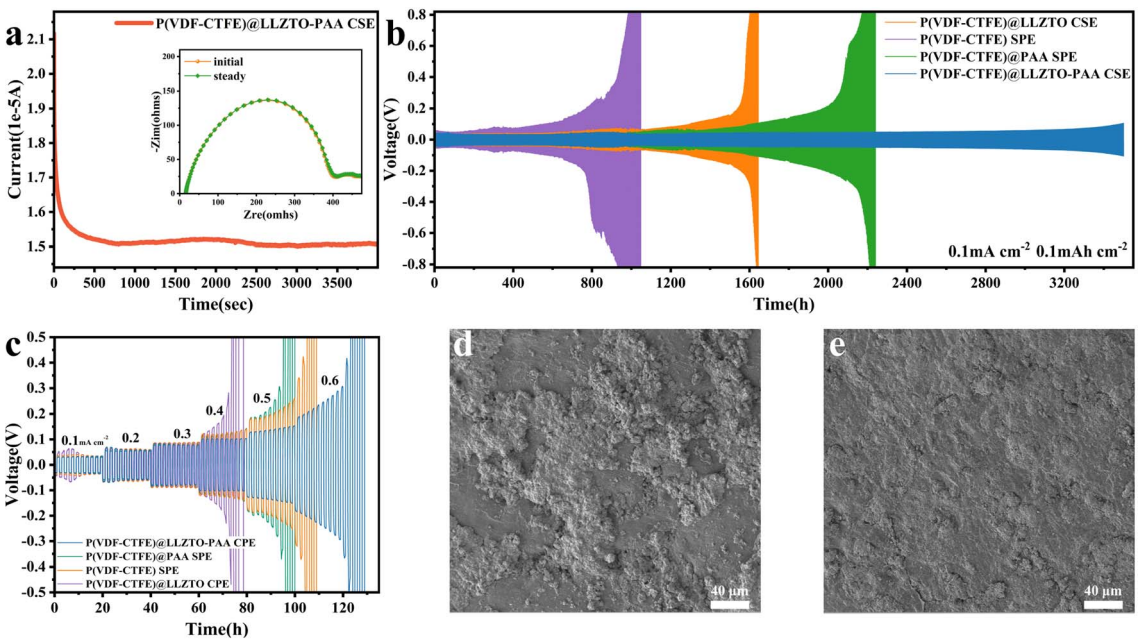

Fig. 5 (a) Chronoamperometry profile of the Li/Li symmetric cell for P(VDF-CTFE)@LLZTO-PAA CSE. The inset shows the EIS curves before and after polarization. (b) Cycling performance of Li||SSEs||Li cells plating/stripping. (c) The critical current density test of Li||SSEs||Li cells. The surface morphologies of lithium metal after 200 h: (d) Li||P(VDF-CTFE) @LLZTO CSE||Li and (e) Li||P(VDF-CTFE)@LLZTO-PAA CSE||Li.

CTFE)@LLZTO-PAA CSE ||Li has a flat surface and uniform lithium deposition. Due to the uneven deposition of lithium, the volume of the interface between the SSE membrane and lithium may change, eventually leading to cell failure.[47,49] These results suggest that adding LLZTO-PAA fillers effectively promotes the uniform diffusion of Li^+ and inhibits lithium dendrite growth between the electrolyte membrane and lithium metal electrode.

2.6. Performance of full cells and Li anode interface stability

To evaluate the practical application of SSEs in lithium metal batteries, LFP||SSEs||Li cells are tested for the electrochemical performance at room temperature. The rate performance of the LFP||SSEs||Li cells is tested across a range of rates, and the corresponding results are presented in Fig. 6(a). The LFP||P(VDF-CTFE)@LLZTO-PAA CSE||Li battery exhibits 164.2, 160.4, 155.2, 147.1, 138.3, 131.3, and 118.8 mA h g^{-1} at rates of 0.1, 0.3, 0.5, 1, 2, 3 and 5C, respectively. After the rate returns to 0.3C, the cell can maintain a reversible capacity of 159.7 mA h g^{-1}. In contrast, the LFP||P(VDF-CTFE)@LLZTO CSE||Li cell exhibits only 154.8, 151.2, 147.5, 139.3, 127.8, 117.1, and 99.2 mA h g^{-1}, respectively, and the discharge capacity is 149.7 mA h g^{-1} after returning to 0.3C. The excellent rate performance of the P(VDF-CTFE)@LLZTO-PAA CSE can be mainly attributed to the high ionic conductivity and t_{Li^+}, and its excellent reversibility indicates that the high rate charging and discharging process does not cause severe damage to the CSE.[51]

Fig. 6(b) demonstrates the cycle performance of the LFP||SSEs||Li cells at a rate of 1C. The initial discharge capacity of the LFP||P(VDF-CTFE)@LLZTO CSE||Li cell is 134.8 mA h g^{-1}. After 250 cycles, the cell exhibits a specific capacity of only 120.5 mA h g^{-1}, retaining 89.4% of its initial capacity. The fluctuations in charge/discharge efficiency in the middle stage probably originate from the breakage and formation of the unstable solid electrolyte interphase (SEI) layer.[49] Notably, the initial specific capacity of the LFP||P(VDF-CTFE)@LLZTO-PAA CSE||Li cell at 1C is 143.8 mA h g^{-1}. Subsequently, the capacity increases to 146.5 mA h g^{-1}. This finding can be attributed to a decrease in interface resistance with further activation of the cell and the homogenization process of the Li^+ in the CSE membrane.[30] Fig. 6(c) exhibits the charge/discharge curves for the LFP||SSEs||Li cells at the 1st cycle and the 250th cycle. More importantly, the LLZTO-PAA-based cell maintains a specific capacity of 131.5 mA h g^{-1} and a capacity retention rate of 91.45% after 650 steady cycles. Furthermore, Fig. S13† shows that the LFP||P(VDF-CTFE)@LLZTO-PAA CSE||Li battery exhibits good cycling performance at 0.3C. It has an initial capacity of

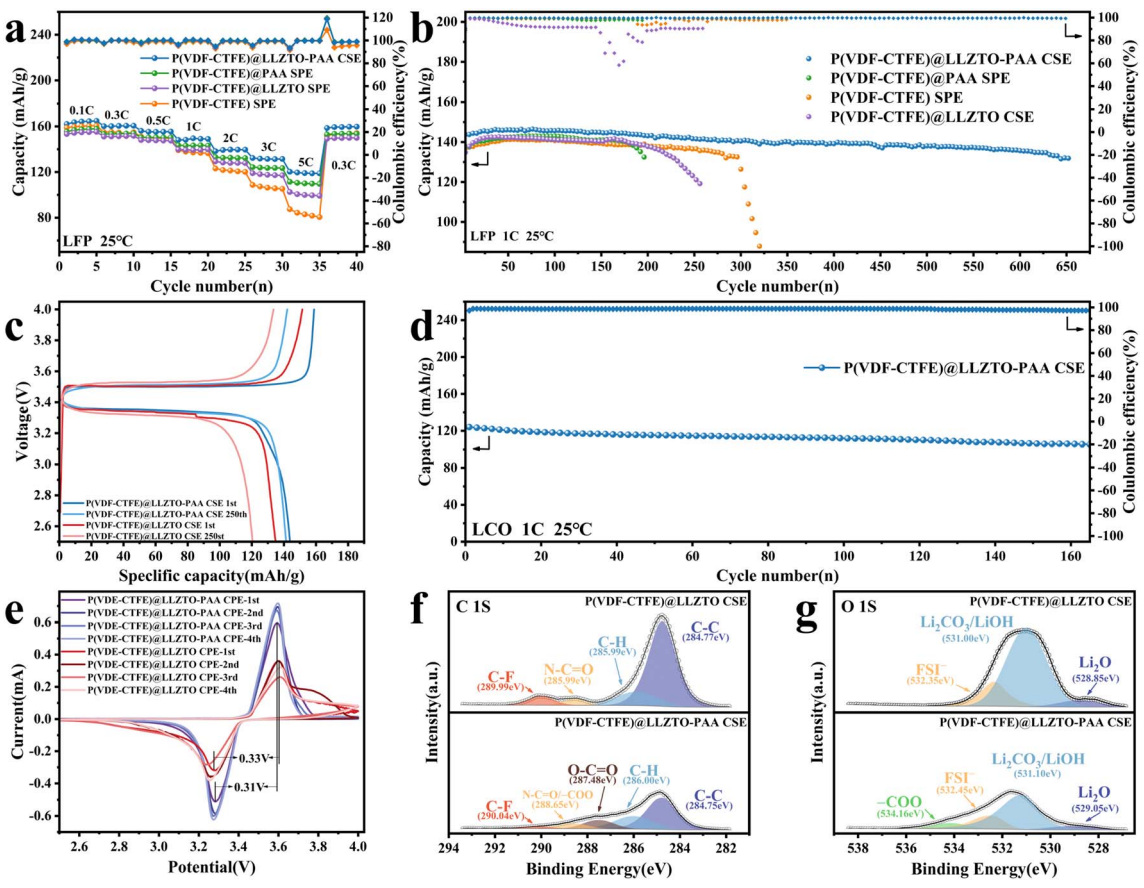

Fig. 6 (a) Rate capacity and (b) long-term cycling performance at 1C of LFP||SSEs||Li cells. (c) The charge/discharge curves of LFP||SSEs||Li cells. (d) Long-term cycling performance at 1C of the LCO||P(VDF-CTFE)@LLZTO-PAA CSE||Li cell. (e) CV curves of the first four cycles of LFP||SSEs||Li cells. XPS spectra of lithium metal anodes from LFP||SSEs||Li after cycling: (f) C 1s and (g) O 1s.

159.4 mA h g^{-1}, and after 505 cycles, the cell also has a capacity of 148.7 mA h g^{-1} and a charge/discharge efficiency of 99.5%. The 4.5 V electrochemical window of the P(VDF-CTFE)@LLZTO-PAA CSE also predicts its ability to match with the high voltage cathode; thus we assemble the electrolyte membrane with LCO to form an LCO‖P(VDF-CTFE) SPE‖Li cell. Fig. 6(d) demonstrates the cycle performance of the LCO‖Li cell at 1C, where the cell has an initial specific capacity of 124.1 mA h g^{-1}, and can cycle for 160 cycles with a capacity retention of 84.9%. These findings demonstrate that the P(VDF-CTFE)@LLZTO-PAA CSE has high reversibility and good electrochemical stability due to the excellent ionic conductivity and homogeneous LLZTO-PAA fillers ensuring uniform Li^+ flux.

To further investigate the changes that occur in the electrolyte membrane during charge and discharge, the LFP‖SSEs‖Li cells are tested using cyclic voltammetry (CV) from 2.5 to 4 V. As shown in Fig. 6(e), the haphazard and non-overlapping curves of the LFP‖P(VDF-CTFE)@LLZTO CSE‖Li cell show the presence of some side reactions in the cell. In contrast, the LFP‖P(VDF-CTFE)@LLZTO-PAA CSE‖Li cell shows good reproducibility in the CV curves of the first four cycles, indicating the improvement of electrochemical stability of the ceramic filler for the electrolyte membrane.[52] The other difference is the voltage difference between the oxidation and reduction peaks in the first cycle, which is 0.33 V for the LFP‖P(VDF-CTFE)@LLZTO CSE‖Li cell and 0.31 V for the LFP‖P(VDF-CTFE)@LLZTO-PAA CSE‖Li cell. This finding suggests that the P(VDF-CTFE)@LLZTO-PAA CSE has better kinetic performance for Li^+ transport.

The LFP‖SSEs‖Li cells are cycled 100 times before testing the lithium anode electrode using XPS to explore the chemistry on the interfacial phase layer (Fig. 6(f and g)). As for the C 1S spectrum of LFP‖P(VDF-CTFE)@LLZTO CSE‖Li, the peaks of C–C (284.77 eV), C–H (285.99 eV), N–C=O (288.60 eV), and C–F (289.99 eV) are observed, which is mainly attributed to the residue and decomposition of the polymer matrix and DMF.[53] N–C=O is mainly derived from the amide group in the residual DMF.[14] But for LFP‖P(VDF-CTFE)@LLZTO-PAA CSE‖Li (N–C=O/–COO: 288.65 eV), the N–C=O of residual DMF solvent and the carboxylate groups (–COO) of polyacrylic acid both produce peaks which overlap at ~288 eV.[54,55] In addition, a new peak is observed at 287.46 eV, which is attributed to the C–C=O of polyacrylic acid.[56] Another difference is found in the O 1S spectra for Li_2O, Li_2CO_3/LiOH and FSI^-, which mainly comes from the reaction of the polymer matrix with lithium and the LiFSI residue.[31,53] Evidently, the peak area of Li_2CO_3/LiOH in LFP‖P(VDF-CTFE)@LLZTO-PAA CSE‖Li is reduced (Fig. S14†) due to the removal of trace amounts of water from the membrane by the absorption effect of the homogeneously dispersed LLZTO-PAA fillers, which mitigates the reaction of the impurities with lithium.[33] In the O 1S spectrum of LFP‖P(VDF-CTFE)@LLZTO-PAA CSE‖Li, the small bump at 354.16 eV is related to the COO^- of polyacrylic acid and its reactants.[55] The areas of peaks of C 1S and O 1S spectra using P(VDF-CTFE)@LLZTO CSE are larger than those using P(VDF-CTFE)@LLZTO-PAA CSE (Fig. S14†), indicating that LLZTO-PAA is more beneficial to inhibit electrolyte decomposition.[14] These results indicate the disparity in the structure and chemical distribution of the SEI of P(VDF-CTFE)@LLZTO-PAA CSE and P(VDF-CTFE)@LLZTO CSE, leading to different cell performances.

3 Conclusion

We found that PAA is more susceptible to redox reactions than P(VDF-CTFE), which is supported by the DFT analysis. Thus, a composite solid-state electrolyte composed of a P(VDF-CTFE) polymer matrix and PAA-modified LLZTO fillers is prepared using the solution casting method. The surficial modification of LLZTO using the PAA sacrificial agent forms a core–shell structure and removes alkaline impurities with low conductivity from the ceramic surface. Therefore, this approach facilitates the reduction of defluorination in P(VDF-CTFE), and ensures the fluidity of the slurry, thus improving the distribution of the fillers in the electrolyte membrane and reducing the degree of agglomeration of LLZTO. As a result, P(VDF-CTFE)@LLZTO-PAA CSE exhibits a high ionic conductivity of 4.53×10^{-4} S cm^{-1} and enhanced electrochemical stability with a window of 4.5 V (*vs.* Li^+/Li) and mechanical properties (5.22 MPa). This transformation can be attributed to the enhancement of the ion transport performance in the CSE membrane by LLZTO-PAA fillers, and the dense structure formed by the filler and polymer matrix, which constructs a continuous Li^+ transport pathway. The homogeneously distributed LLZTO-PAA fillers endow the Li‖P(VDF-CTFE)@LLZTO-PAA CSE‖Li cell with uniform lithium plating/stripping and enhanced suppression of lithium dendrites, enabling stable cycling for up to 3500 h. The LFP‖P(VDF-CTFE)@LLZTO-PAA CSE‖Li cell demonstrates excellent rate performance and enhanced cycling stability. In addition, the LCO‖P(VDF-CTFE)@LLZTO-PAA CSE‖Li cell also shows the potential of CSE to match with the high voltage cathode. This study provides a facile strategy for improving the distribution of ceramic fillers in the polymeric matrix, while contributing to the large-scale industrial fabrication of organic/inorganic composite solid-state electrolytes.

Data availability

Data will be made available on request.

Author contributions

Bin Luo: investigation, data curation, writing – original draft. Jintian Wu: writing – review & editing, methodology. Ming Zhang: software, visualization. Zhihao Zhang: data curation, investigation. Xingwei Zhang: methodology, visualization. Zixuan Fang: conceptualization, writing – review & editing. Ziqiang Xu: conceptualization, supervision. Mengqiang Wu: conceptualization, resources.

Conflicts of interest

The authors declare no conflict of interest.

Acknowledgements

This work was supported by the National Natural Science Foundation of China (Grant No. 52102123) and Natural Science Foundation of Sichuan Province (Grant No. 2022NSFSC2008 and Grant No. 2023NSFSC0442).

Notes and references

1 X. Ji, Y. Zhang, M. Cao, Q. Gu, H. Wang, J. Yu, Z.-H. Guo and X. Zhou, Advanced inorganic/polymer hybrid electrolytes for all-solid-state lithium batteries, *J. Adv. Ceram.*, 2022, **11**, 835–861.

2 H. J. Ban, M.-Y. Kim, S.-J. Park, B.-S. Kang, J. Lim, Y. Hong, S. H. Yang and H.-S. Kim, Electrochemical behavior of rutile phase TiO_2-coated NCM materials for ASLBs operated at a high temperature, *Surf. Coat. Technol.*, 2022, **430**, 127984.

3 L. Chen, Y. Li, S.-P. Li, L.-Z. Fan, C.-W. Nan and J. B. Goodenough, PEO/garnet composite electrolytes for solid-state lithium batteries: From "ceramic-in-polymer" to "polymer-in-ceramic", *Nano Energy*, 2018, **46**, 176–184.

4 Z. Cai, R. Xiao and B. Jiang, Architecting with a flexible and modified polyethylene oxide coating for ambient-temperature solid-state Li metal batteries, *Surf. Coat. Technol.*, 2021, **421**, 127389.

5 L. Chen, X. Qiu, Z. Bai and L.-Z. Fan, Enhancing interfacial stability in solid-state lithium batteries with polymer/garnet solid electrolyte and composite cathode framework, *J. Energy Chem.*, 2021, **52**, 210–217.

6 Y.-F. Huang, T. Gu, G. Rui, P. Shi, W. Fu, L. Chen, X. Liu, J. Zeng, B. Kang, Z. Yan, F. J. Stadler, L. Zhu, F. Kang and Y.-B. He, A relaxor ferroelectric polymer with an ultrahigh dielectric constant largely promotes the dissociation of lithium salts to achieve high ionic conductivity, *Energy Environ. Sci.*, 2021, **14**, 6021–6029.

7 N. Yao, X. Chen, X. Shen, R. Zhang, Z. H. Fu, X. X. Ma, X. Q. Zhang, B. Q. Li and Q. Zhang, An Atomic Insight into the Chemical Origin and Variation of the Dielectric Constant in Liquid Electrolytes, *Angew Chem. Int. Ed. Engl.*, 2021, **60**, 21473–21478.

8 S. Lee, K.-s. Lee, S. Kim, K. Yoon, S. Han, M. H. Lee, Y. Ko, J. H. Noh, W. Kim and K. Kang, Design of a lithiophilic and electron-blocking interlayer for dendrite-free lithium-metal solid-state batteries, *Sci. Adv.*, 2022, **8**, eabq0153.

9 H. Huo, J. Luo, V. Thangadurai, X. Guo, C.-W. Nan and X. Sun, Li_2CO_3: a Critical Issue for Developing Solid Garnet Batteries, *ACS Energy Lett.*, 2019, **5**, 252–262.

10 Y. Li, X. Chen, A. Dolocan, Z. Cui, S. Xin, L. Xue, H. Xu, K. Park and J. B. Goodenough, Garnet Electrolyte with an Ultralow Interfacial Resistance for Li-Metal Batteries, *J. Am. Chem. Soc.*, 2018, **140**, 6448–6455.

11 W. M. Seong, Y. Kim and A. Manthiram, Impact of Residual Lithium on the Adoption of High-Nickel Layered Oxide Cathodes for Lithium-Ion Batteries, *Chem. Mater.*, 2020, **32**, 9479–9489.

12 S. S. Zhang, Problems and their origins of Ni-rich layered oxide cathode materials, *Energy Storage Mater.*, 2020, **24**, 247–254.

13 H. Sheng, X. H. Meng, D. D. Xiao, M. Fan, W. P. Chen, J. Wan, J. Tang, Y. G. Zou, F. Wang, R. Wen, J. L. Shi and Y. G. Guo, An Air-Stable High-Nickel Cathode with Reinforced Electrochemical Performance Enabled by Convertible Amorphous Li_2CO_3 Modification, *Adv. Mater.*, 2022, **34**, e2108947.

14 K. Yang, L. Chen, J. Ma, C. Lai, Y. Huang, J. Mi, J. Biao, D. Zhang, P. Shi, H. Xia, G. Zhong, F. Kang and Y. B. He, Stable Interface Chemistry and Multiple Ion Transport of Composite Electrolyte Contribute to Ultra-long Cycling Solid-State $LiNi_{0.8}Co_{0.1}Mn_{0.1}O_2$/Lithium Metal Batteries, *Angew Chem. Int. Ed. Engl.*, 2021, **60**, 24668–24675.

15 X. Yi, Y. Guo, S. Chi, S. Pan, C. Geng, M. Li, Z. Li, W. Lv, S. Wu and Q. H. Yang, Surface Li_2CO_3 Mediated Phosphorization Enables Compatible Interfaces of Composite Polymer Electrolyte for Solid-State Lithium Batteries, *Adv. Funct. Mater.*, 2023, **33**, 2303574.

16 R.-A. Tong, L. Chen, B. Fan, G. Shao, R. Liu and C.-A. Wang, Solvent-Free Process for Blended PVDF-HFP/PEO and LLZTO Composite Solid Electrolytes with Enhanced Mechanical and Electrochemical Properties for Lithium Metal Batteries, *ACS Appl. Energy Mater.*, 2021, **4**, 11802–11812.

17 H. Huo, Y. Chen, N. Zhao, X. Lin, J. Luo, X. Yang, Y. Liu, X. Guo and X. Sun, In-situ formed Li_2CO_3-free garnet/Li interface by rapid acid treatment for dendrite-free solid-state batteries, *Nano Energy*, 2019, **61**, 119–125.

18 H. Huo, X. Li, Y. Sun, X. Lin, K. Doyle-Davis, J. Liang, X. Gao, R. Li, H. Huang, X. Guo and X. Sun, Li_2CO_3 effects: New insights into polymer/garnet electrolytes for dendrite-free solid lithium batteries, *Nano Energy*, 2020, **73**, 104836.

19 Z. Qin, Y. Xie, X. Meng, D. Qian, C. Shan, D. Mao, G. He, Z. Zheng, L. Wan and Y. Huang, Interface engineering for garnet-type electrolyte enables low interfacial resistance in solid-state lithium batteries, *Chem. Eng. J.*, 2022, **447**, 137538.

20 M. J. Lee, D. O. Shin, J. Y. Kim, J. Oh, S. H. Kang, J. Kim, K. M. Kim, Y. M. Lee, S. O. Kim and Y.-G. Lee, Interfacial barrier free organic-inorganic hybrid electrolytes for solid state batteries, *Energy Storage Mater.*, 2021, **37**, 306–314.

21 Z. Huang, R.-a. Tong, J. Zhang, L. Chen and C.-A. Wang, Blending Poly(ethylene oxide) and $Li_{6.4}La_3Zr_{1.4}Ta_{0.6}O_{12}$ by Haake Rheomixer without any solvent: A low-cost manufacture method for mass production of composite polymer electrolyte, *J. Power Sources*, 2020, **451**, 227797.

22 J. DONG, Y. OZAKI and K. NAKASHIMA, FTIR Studies of Conformational Energies of Poly(acrylic Acid) in Cast Films, *J. Polym. Sci., Part B: Polym. Phys.*, 1996, **35**, 507–515.

23 L. Tonghuan, D. Guojian, D. Xiaojiang, W. Wangsuo and Y. Ying, Adsorptive features of polyacrylic acid hydrogel for UO_2^{2+}, *J. Radioanal. Nucl. Chem.*, 2012, **297**, 119–125.

24 S. Komaba, K. Shimomura, N. Yabuuchi, T. Ozeki, H. Yui and K. Konno, Study on Polymer Binders for High-Capacity SiO Negative Electrode of Li-Ion Batteries, *J. Phys. Chem. C*, 2011, **115**, 13487–13495.

25 M. Todica, R. Stefan, C. V. Pop and L. Olar, IR and Raman Investigation of Some Poly(acrylic) Acid Gels in Aqueous and Neutralized State, *Acta Phys. Pol., A*, 2015, **128**, 128–135.
26 A. Joachimiak, L. Okrasa, T. Halamus and P. Wojciechowski, Stabilisation Effect of Calcium Ions on Polymer Network in Hydrogels Derived from a Lyotropic Phase of Hydroxypropylcellulose, *Macromol. Symp.*, 2005, **222**, 203–208.
27 P. Zhang, B. Han, X. Yang, Y. Zou, X. Lu, X. Liu, Y. Zhu, D. Wu, S. Shen, L. Li, Y. Zhao, J. S. Francisco and M. Gu, Revealing the Intrinsic Atomic Structure and Chemistry of Amorphous LiO_2-Containing Products in Li-O_2 Batteries Using Cryogenic Electron Microscopy, *J. Am. Chem. Soc.*, 2022, **144**, 2129–2136.
28 W. M. Seong, K. H. Cho, J. W. Park, H. Park, D. Eum, M. H. Lee, I. S. Kim, J. Lim and K. Kang, Controlling Residual Lithium in High-Nickel (>90%) Lithium Layered Oxides for Cathodes in Lithium-Ion Batteries, *Angew Chem. Int. Ed. Engl.*, 2020, **59**, 18662–18669.
29 X. Zhang, T. Liu, S. Zhang, X. Huang, B. Xu, Y. Lin, B. Xu, L. Li, C. W. Nan and Y. Shen, Synergistic Coupling between $Li_{6.75}Li_3Zr_{1.75}Ta_{0.25}O_{12}$ and Poly(vinylidene fluoride) Induces High Ionic Conductivity, Mechanical Strength, and Thermal Stability of Solid Composite Electrolytes, *J. Am. Chem. Soc.*, 2017, **139**, 13779–13785.
30 L. Liu, D. Zhang, J. Zhao, J. Shen, F. Li, Y. Yang, Z. Liu, W. He, W. Zhao and J. Liu, Synergistic Effect of Lithium Salts with Fillers and Solvents in Composite Electrolytes for Superior Room-Temperature Solid-State Lithium Batteries, *ACS Appl. Energy Mater.*, 2022, **5**, 2484–2494.
31 C. Xue, X. Zhang, S. Wang, L. Li and C. W. Nan, Organic-Organic Composite Electrolyte Enables Ultralong Cycle Life in Solid-State Lithium Metal Batteries, *ACS Appl. Mater. Interfaces*, 2020, **12**, 24837–24844.
32 L. Zheng, J. Wang, D. Yu, Y. Zhang and Y. Wei, Preparation of PVDF-CTFE hydrophobic membrane by non-solvent induced phase inversion: Relation between polymorphism and phase inversion, *J. Membr. Sci.*, 2018, **550**, 480–491.
33 J. Zhang, Y. Zeng, Q. Li, Z. Tang, D. Sun, D. Huang, L. Zhao, Y. Tang and H. Wang, Polymer-in-salt electrolyte enables ultrahigh ionic conductivity for advanced solid-state lithium metal batteries, *Energy Storage Mater.*, 2023, **54**, 440–449.
34 W. Liu, C. Yi, L. Li, S. Liu, Q. Gui, D. Ba, Y. Li, D. Peng and J. Liu, Designing Polymer-in-Salt Electrolyte and Fully Infiltrated 3D Electrode for Integrated Solid-State Lithium Batteries, *Angew. Chem., Int. Ed.*, 2021, **60**, 12931–12940.
35 C. Ribeiro, C. M. Costa, D. M. Correia, J. Nunes-Pereira, J. Oliveira, P. Martins, R. Goncalves, V. F. Cardoso and S. Lanceros-Mendez, Electroactive poly(vinylidene fluoride)-based structures for advanced applications, *Nat. Protoc.*, 2018, **13**, 681–704.
36 J. Zhang, X. Zang, H. Wen, T. Dong, J. Chai, Y. Li, B. Chen, J. Zhao, S. Dong, J. Ma, L. Yue, Z. Liu, X. Guo, G. Cui and L. Chen, High-voltage and free-standing poly(propylene carbonate)/$Li_{6.75}La_3Zr_{1.75}Ta_{0.25}O_{12}$ composite solid electrolyte for wide temperature range and flexible solid lithium ion battery, *J. Mater. Chem. A*, 2017, **5**, 4940–4948.
37 A. Bottino, G. Capannelli, O. Monticelli and P. Piaggio, Poly(vinylidene fluoride) with improved functionalization for membrane production, *J. Membr. Sci.*, 2000, **166**, 23–29.
38 S. Zhang, J. Shen, X. Qiu, D. Weng and W. Zhu, ESR and vibrational spectroscopy study on poly(vinylidene fluoride) membranes with alkaline treatment, *J. Power Sources*, 2006, **153**, 234–238.
39 L. Peng, Z. Lu, L. Zhong, J. Jian, Y. Rong, R. Yang, Y. Xu and C. Jin, Enhanced ionic conductivity and interface compatibility of PVDF-LLZTO composite solid electrolytes by interfacial maleic acid modification, *J. Colloid Interface Sci.*, 2022, **613**, 368–375.
40 Q. Zhou, J. Ma, S. Dong, X. Li and G. Cui, Intermolecular Chemistry in Solid Polymer Electrolytes for High-Energy-Density Lithium Batteries, *Adv. Mater.*, 2019, **31**, e1902029.
41 J. Zheng and Y.-Y. Hu, New Insights into the Compositional Dependence of Li-Ion Transport in Polymer–Ceramic Composite Electrolytes, *ACS Appl. Mater. Interfaces*, 2018, **10**, 4113–4120.
42 C. Bai, Z. Wu, W. Xiang, G. Wang, Y. Liu, Y. Zhong, B. Chen, R. Liu, F. He and X. Guo, Poly(ethylene oxide)/Poly(vinylidene fluoride)/$Li_{6.4}La_3Zr_{1.4}Ta_{0.6}O_{12}$ composite electrolyte with a stable interface for high performance solid state lithium metal batteries, *J. Power Sources*, 2020, **472**, 228461.
43 L. Bi, X. Wei, Y. Qiu, Y. Song, X. Long, Z. Chen, S. Wang and J. Liao, A highly ionic transference number eutectogel hybrid electrolytes based on spontaneous coupling inhibitor for solid-state lithium metal batteries, *Nano Res.*, 2022, **16**, 1717–1725.
44 X. Zhang, J. Han, X. Niu, C. Xin, C. Xue, S. Wang, Y. Shen, L. Zhang, L. Li and C. W. Nan, High Cycling Stability for Solid-State Li Metal Batteries via Regulating Solvation Effect in Poly(Vinylidene Fluoride)-Based Electrolytes, *Batteries Supercaps*, 2020, **3**, 876–883.
45 J. Zhang, N. Zhao, M. Zhang, Y. Li, P. K. Chu, X. Guo, Z. Di, X. Wang and H. Li, Flexible and ion-conducting membrane electrolytes for solid-state lithium batteries: Dispersion of garnet nanoparticles in insulating polyethylene oxide, *Nano Energy*, 2016, **28**, 447–454.
46 J. Mi, J. Ma, L. Chen, C. Lai, K. Yang, J. Biao, H. Xia, X. Song, W. Lv, G. Zhong and Y.-B. He, Topology crafting of polyvinylidene difluoride electrolyte creates ultra-long cycling high-voltage lithium metal solid-state batteries, *Energy Storage Mater.*, 2022, **48**, 375–383.
47 Z. Zhang, S. Zhang, S. Geng, S. Zhou, Z. Hu and J. Luo, Agglomeration-free composite solid electrolyte and enhanced cathode-electrolyte interphase kinetics for all-solid-state lithium metal batteries, *Energy Storage Mater.*, 2022, **51**, 19–28.
48 Q. Guo, F. Xu, L. Shen, Z. Wang, J. Wang, H. He and X. Yao, Poly(ethylene glycol) brush on $Li_{6.4}La_3Zr_{1.4}Ta_{0.6}O_{12}$ towards intimate interfacial compatibility in composite polymer electrolyte for flexible all-solid-state lithium metal batteries, *J. Power Sources*, 2021, **498**, 229934.

49 L. Tan, Y. Sun, C. Wei, Y. Tao, Y. Tian, Y. An, Y. Zhang, S. Xiong and J. Feng, Design of Robust, Lithiophilic, and Flexible Inorganic-Polymer Protective Layer by Separator Engineering Enables Dendrite-Free Lithium Metal Batteries with LiNi0.8 Mn0.1 Co0.1 O2 Cathode, *Small*, 2021, **17**, e2007717.

50 J. Y. Liang, X. X. Zeng, X. D. Zhang, T. T. Zuo, M. Yan, Y. X. Yin, J. L. Shi, X. W. Wu, Y. G. Guo and L. J. Wan, Engineering Janus Interfaces of Ceramic Electrolyte via Distinct Functional Polymers for Stable High-Voltage Li-Metal Batteries, *J. Am. Chem. Soc.*, 2019, **141**, 9165–9169.

51 X. Zheng, J. Wu, X. Wang and Z. Yang, Cellulose-reinforced poly(cyclocarbonate-ether)-based composite polymer electrolyte and facile gel interfacial modification for solid-state lithium-ion batteries, *Chem. Eng. J.*, 2022, **446**, 137194.

52 H. Wang, C. Lin, X. Yan, A. Wu, S. Shen, G. Wei and J. Zhang, Mechanical property-reinforced PEO/PVDF/$LiClO_4$/SN blend all solid polymer electrolyte for lithium ion batteries, *J. Electroanal. Chem.*, 2020, **869**, 114156.

53 X. Zhang, S. Wang, C. Xue, C. Xin, Y. Lin, Y. Shen, L. Li and C. W. Nan, Self-Suppression of Lithium Dendrite in All-Solid-State Lithium Metal Batteries with Poly(vinylidene difluoride)-Based Solid Electrolytes, *Adv. Mater.*, 2019, **31**, e1806082.

54 K. Yang, L. Chen, J. Ma, C. Lai, Y. Huang, J. Mi, J. Biao, D. Zhang, P. Shi, H. Xia, G. Zhong, F. Kang and Y. B. He, Stable Interface Chemistry and Multiple Ion Transport of Composite Electrolyte Contribute to Ultra-long Cycling Solid-State $LiNi_{0.8}Co_{0.1}Mn_{0.1}O_2$/Lithium Metal Batteries, *Angew. Chem., Int. Ed.*, 2021, **60**, 24668–24675.

55 B. Sun, M. El Kazzi, E. Müller and E. J. Berg, Toward high-performance $Li(Ni_xCo_yMn_z)O_2$ cathodes: facile fabrication of an artificial polymeric interphase using functional polyacrylates, *J. Mater. Chem. A*, 2018, **6**, 17778–17786.

56 R. Dong, M. Lindau and C. K. Ober, Dissociation Behavior of Weak Polyelectrolyte Brushes on a Planar Surface, *Langmuir*, 2009, **25**, 4774–4779.